JGR Solid Earth

RESEARCH ARTICLE
10.1029/2021JB022167

Evidence of Volatile-Induced Melting in the Northeast Asian Upper Mantle

Yizhuo Sun[1,2,3,4], Saswata Hier-Majumder[2,5], Benoit Tauzin[6,7], Michael Walter[8], Maxim Ballmer[9], Yigang Xu[1,3], and Seongryong Kim[10]

[1]State Key Laboratory of Isotope Geochemistry, Guangzhou Institute of Geochemistry, Chinese Academy of Sciences, Guangzhou, China, [2]Department of Earth Sciences, Royal Holloway University of London, Egham, UK, [3]CAS Center for Excellence in Deep Earth Science, Guangzhou, China, [4]University of Chinese Academy of Sciences, Beijing, China, [5]Department of Energy, AAAS Science and Technology Policy Fellow, Advanced Scientific Computing Research, Germantown, MD, USA, [6]Université de Lyon, Université Claude Bernard Lyon 1, Ecole Normale Supérieure de Lyon, Université Jean Monnet, CNRS, LGL-TPE, Villeurbanne, France, [7]Research School of Earth Sciences, Australian National University, Canberra, ACT, Australia, [8]Earth and Planets Laboratory, Carnegie Institution for Science, Washington DC, WA, USA, [9]Department of Earth Sciences, University College London, London, UK, [10]Department of Earth and Environmental Sciences, Korea University, Seoul, Republic of Korea

Key Points:

- The northeast Asian low velocity layer (LVL) is characterized by an average of 0.8 ± 0.5 vol% melt
- It can take 40–80 Ma for the slab-derived carbonate-rich melt channels to reach the LVL top
- Long term interaction between the CO_2-rich melt and the mantle can produce a high μ (HIMU)-like source component

Supporting Information:

Supporting Information may be found in the online version of this article.

Correspondence to:

Y. Sun,
Yizhuo.Sun.2017@live.rhul.ac.uk

Citation:

Sun, Y., Hier-Majumder, S., Tauzin, B., Walter, M., Ballmer, M., Xu, Y., & Kim, S. (2021). Evidence of volatile-induced melting in the northeast Asian upper mantle. *Journal of Geophysical Research: Solid Earth*, *126*, e2021JB022167. https://doi.org/10.1029/2021JB022167

Received 7 APR 2021
Accepted 27 SEP 2021

Abstract A seismic low velocity layer (LVL) above the mantle transition zone (MTZ), often thought to be caused by volatile-induced melting, can significantly modulate planetary volatile cycles. In this work, we show that an LVL observed beneath northeast Asia is characterized by small, 0.8 ± 0.5 vol%, average degrees of partial melting. Seismically derived P-T conditions of the LVL indicate that slab-derived CO_2, possibly combined with small amounts of H_2O, is necessary to induce melting. Modeling the reactive infiltration instability of the melt in a stationary mantle above a stalled slab, we demonstrate that the volatile-rich melt slowly rises above the stalled slab in the MTZ, with percolation velocities of 200–500 μm/yr. The melt remains stable within the LVL for this geologically significant period of time, potentially transferring up to 52 Mt/yr of CO_2 from the subducting slab to the mantle for an LVL similar in areal extent (3.4×10^6 km^2) to the northeast Asian LVL. Reaction between the melt channels and the LVL mantle precipitates up to 200 ppmw solid C in localized zones. Using the inferred small melt volume fraction to model trace element abundances and isotopic signatures, we show that interaction between this melt and the surrounding mantle can over the long-term produce rocks bearing a HIMU like geochemical signature.

Plain Language Summary Volatile elements, such as hydrogen and carbon, are elements that can be condensed only at low temperatures. As a small amount of these volatiles can apparently lower the solidus and viscosity of mantle rocks, they are intuitively implied to play an important role in the upper mantle dynamics. Our study focuses on the northeast Asian low-velocity layer (LVL), a layer of 61 ± 15 km above the mantle transition zone marked by a 2%–3% reduction in shear wave velocity. We integrated multiple methods and techniques, including rock physics analysis of seismology, numerical simulation of porous flow, and geochemical modeling. Our rock physics analysis suggests the LVL as a potential deep volatile (carbon and/or hydrogen) reservoir, containing 0.8 ± 0.5 vol% melt. Our simulations predict that the LVL can transfer up to 52 Mt/yr of CO_2 to the overlying mantle. This study presents a research model of qualitative analyses and quantitative measurements of the deep volatile cycling, providing a direction for the deep volatile study in other tectonic environments.

1. Introduction

Since the first discovery by Revenaugh and Sipkin (1994) from multiple-ScS reverberation mapping in northeast Asia, a seismic low velocity layer (LVL) above the mantle transition zone (MTZ) has been observed with a thickness ranging from ~20 to 90 km in a number of tectonic settings, including convergent oceanic margins, plume, and continental collision zones (Tauzin et al., 2010; Vinnik & Farra, 2007; Wei & Shearer, 2017). Seismological methods used to detect such a LVL range from multiple-ScS reverberations (Bagley et al., 2009; Courtier & Revenaugh, 2007; Revenaugh & Sipkin, 1994), receiver functions (Liu et al., 2016; Tauzin et al., 2010, 2017; Vinnik & Farra, 2002, 2007), SS precursors (Wei & Shearer, 2017), body

wave triplications (Gao et al., 2006; Han et al., 2021; Song et al., 2004), and seismic tomography (Obayashi et al., 2006). Marked by a sharp interface with the overlying mantle and a 2%–6% reduction in shear wave velocity, the LVL is generally recognized as a chemical, rather than thermal, anomaly. A number of recent rock physics analyses suggest that the LVL is characterized by an average of 0.5–1 vol% partial melt embedded in a silicate matrix (Freitas et al., 2017; Hier-Majumder & Courtier, 2011; Hier-Majumder & Tauzin, 2017; Hier-Majumder et al., 2014; Xiao et al., 2020). While it is plausible that the LVL is a global phenomenon (Tauzin et al., 2010), the highest resolution of its internal structure is obtained from regional studies, such as in the western US (Eagar et al., 2010; Fee & Dueker, 2004; Hier-Majumder & Tauzin, 2017; Jasbinsek & Dueker, 2007; Jasbinsek et al., 2010; Schmandt & Humphreys, 2011; Song et al., 2004; Tauzin et al., 2013) and northeast Asia (Bagley et al., 2009; Han et al., 2021; Revenaugh & Sipkin, 1994; Liu et al., 2016). Especially useful in this respect are seismic results obtained from receiver function studies that, in addition to the reduction in shear wave velocities, provide information regarding the thickness of the MTZ (Chevrot et al., 1999; Lawrence & Shearer, 2006; Tauzin et al., 2008). Exploiting the Clapeyron slopes of phase transitions of olivine polymorphs, the MTZ thickness can be converted into mantle temperature, thus providing an additional set of constraints on the physical properties of mantle aggregates. These conversions indicate that the average temperature of the LVLs is far below the solidus of dry peridotite but is closer to the solidi of carbonated basalt and hydrated peridotite (Hier-Majumder & Tauzin, 2017; Sun, Hier-Majumder, et al., 2020), suggesting the presence of volatiles in the melting process.

Partial melting in the LVL bears significant implications for global volatile cycles. Global estimates suggest that between 80–176 Mt/yr (Dasgupta & Hirschmann, 2010) and 300 ± 50 Mt/yr (Plank & Manning, 2019) CO_2 is transmitted to the mantle by subduction. Earth's mantle can be divided at minimum into a depleted MORB source and an enriched OIB source. Estimates from Hirschmann and Dasgupta (2009) indicate that the mantle OIB source contains between 33–500 ppm C and 40–100 ppm H and the MORB source contains 7–25 ppm C and 6–15 ppm H. While a large portion of H_2O and CO_2 are returned to the surface through subduction zone devolatilization and volcanism (Kelemen & Manning, 2015; Plank & Manning, 2019; Plank et al., 2013), some amount survives beyond the volcanic front (Gorman et al., 2006; van Keken et al., 2011). Both H_2O and CO_2 behave as incompatible elements during melting (Dasgupta & Dixon, 2009; Hirschmann, 2006) such that substantial amounts of these volatiles can be stored in the small degree melts observed in the LVL.

Petrological and geochemical evidences provided by sub-lithospheric diamonds (Harte, 2010; Shirey et al., 2021; Walter et al., 2008) and Cenozoic basalts from eastern Asia (Qian et al., 2020) record volatile subduction beyond the volcanic front to the transition zone and lower mantle (Shirey et al., 2021). Carbon and oxygen isotopic anomalies in the sublithospheric diamonds (Burnham et al., 2015; Ickert et al., 2015; Thomson et al., 2014), and Mg isotopic anomaly in basalts (S. Li et al., 2017) demonstrate that slab-derived, volatile-rich fluids interact with the surrounding mantle, producing diamonds and magmas bearing a slab signature. Clinopyroxenes from late Cenozoic Wudi lavas in eastern China reveal the presence of a HIMU (high $^{238}U/^{204}Pb$ ratio) component in the source of these lavas. Geochemical analyses also reveal that these basaltic melts are likely derived from partial melting of carbonated peridotites (Qian et al., 2020). While these petrological and geochemical observations require a reservoir of volatile-rich melts in the mantle, and the rock physics analyses suggest the LVL as a potential candidate, the efficiency of the LVL in sequestering volatiles still remains debated. Additionally, the seismic evidence of melting provides a snapshot in time, lacking constraints on the temporal evolution of volatile-rich melt and reactions between these melts and the mantle.

In this article, we carry out the following steps to quantify the LVL observed beneath northeast Asia. First, we conduct a new rock physics interpretation of published seismic data to yield an estimate of the melt volume fraction in the LVL in Section 2. Then, we compare seismic observations of the observed depth and inferred temperature from both the western and eastern Pacific margins with solidi of volatile-rich and dry mantle assemblages to determine the feasibility of volatile-induced melting in Section 3. Next, we use the seismically inferred melt volume fraction to model modes and timescales of reactive transport of carbonate-rich melts in an LVL in Section 4. Furthermore, based on the inferred melt volume fraction, we model the possible trace element abundances and isotopic signatures resulting from carbonate-rich melts in the LVL and compared them with the concentrations of these elements in natural lavas and xenoliths in Section 5.

Finally, we present the discussions and our conclusions in Section 6. Given the diversity of techniques employed in this study, we provide a short description of each step in the main article, and provide more detailed description of methods and additional results, when appropriate, in the Supporting Information S1.

2. Calculating the Melt Fraction

In this article, we analyze the seismic signals of *P*-to-*S* wave conversions above the northeast Asian MTZ. In the following two subsections, we present a brief description of the methods of seismic data collection and rock physics inversion to calculate the melt fraction of the LVL.

2.1. Seismic Data

The seismic data on the amplitude and depth of *P*-to-*S* (Ps) conversions are derived from Tauzin et al. (2017) for the western margin of the Pacific. We present a detailed description of the steps involved in the seismic data processing, picking, reconstruction of spatial variations, and detections, in the Supporting Information S1. This material also outlines the statistics of absolute depths and amplitudes over the region. We reconstruct the structure of the LVL from the analysis of Ps conversions recorded in the *P*-wave coda of teleseismic earthquakes (Langston, 1979; Vinnik, 1977). Far away from the source, *P*-waves arrive close to the surface approximately as a plane-wave with a steep incidence. These *P*-waves convert a few percent of their energy into shear waves at local discontinuities in elastic properties underneath the receivers. The amplitude of Ps conversions roughly relates to the shear wave velocity contrast across the discontinuity, whereas the time difference between the *P*-wave and Ps conversion gives information about the depth of conversion. Constraints on the thickness of the LVL and wave velocities within the layer come from the differential analysis of travel-times and amplitudes of Ps conversions from the top and the bottom of the LVL (the olivine-wadsleyite transition at 410 km depth). Local *P*-*T* conditions are also obtained from the analysis of the temperature-dependence of phase transitions in the MTZ.

The seismic processing workflow turns individual seismic records from earthquakes into a data cube containing amplitudes of Ps converted waves in the spatial domain. We reconstruct the structure over a grid ranging from 34°N to 49°N in latitude and 115°E–145°E in longitude, with a cell dimension of 0.5° × 0.5°. The spatial extent of this reconstructed grid is shown in the map of MTZ depth in Figure 1a. The seismic section shown in Figure 1b is a representative image of conversion amplitudes in this data cube, along the A-a profile at 37°N. Yellow colors mark positive amplitudes associated with sharp increases of seismic wave velocities such as at the 410-km discontinuity. Blue colors mark negative amplitudes associated with reductions of shear-wave velocities with depth. We use an automated method (see Supporting Information S1) to locate the negative LVL peaks within a depth range of 300–410 km (red dots in Figure 1c) and positive amplitudes indicating the top of the MTZ within a depth range of 360–450 km (blue dots in Figure 1c). Along the cross section in Figure 1c, the thickest part of the LVL beneath northeast Asia appears around the subducting slab, especially seaward on the underside of the subducting slab. This observation is spatially related with the deeper than average 410-km discontinuity at the exact same location, and is consistent with earlier interpretation of higher than normal temperatures from seismic tomography (Obayashi et al., 2006). Our seismic processing leads to a total of 1,490 data points on the grid with information on the amplitude of Ps conversions above the LVL, 410-km discontinuity, and 660-km discontinuity. This data set also contains the depths at which these peaks were observed, from which we calculate the MTZ thickness. In Section 2.2, we discuss how two independent seismically derived constraints, the normalized amplitude of Ps conversion above the LVL and the MTZ thickness, allow us to separate the thermal and chemical signatures of the anomaly.

We further filter the seismically processed data to retain only the most robust signals. To select these signals, we eliminate data points where the peaks of the LVL and the 410 km discontinuity are less than 10 km apart. We then discard points where the 410 km discontinuity was undetected, or detected with an amplitude below a threshold level of 0.5%. This typically occurs in areas with poor data coverage on the sides of the analyzed region. Next, we select data points where the absolute amplitude is higher than the standard error on amplitude for the top of the LVL. We also repeat this data filtering for the top of the MTZ. This

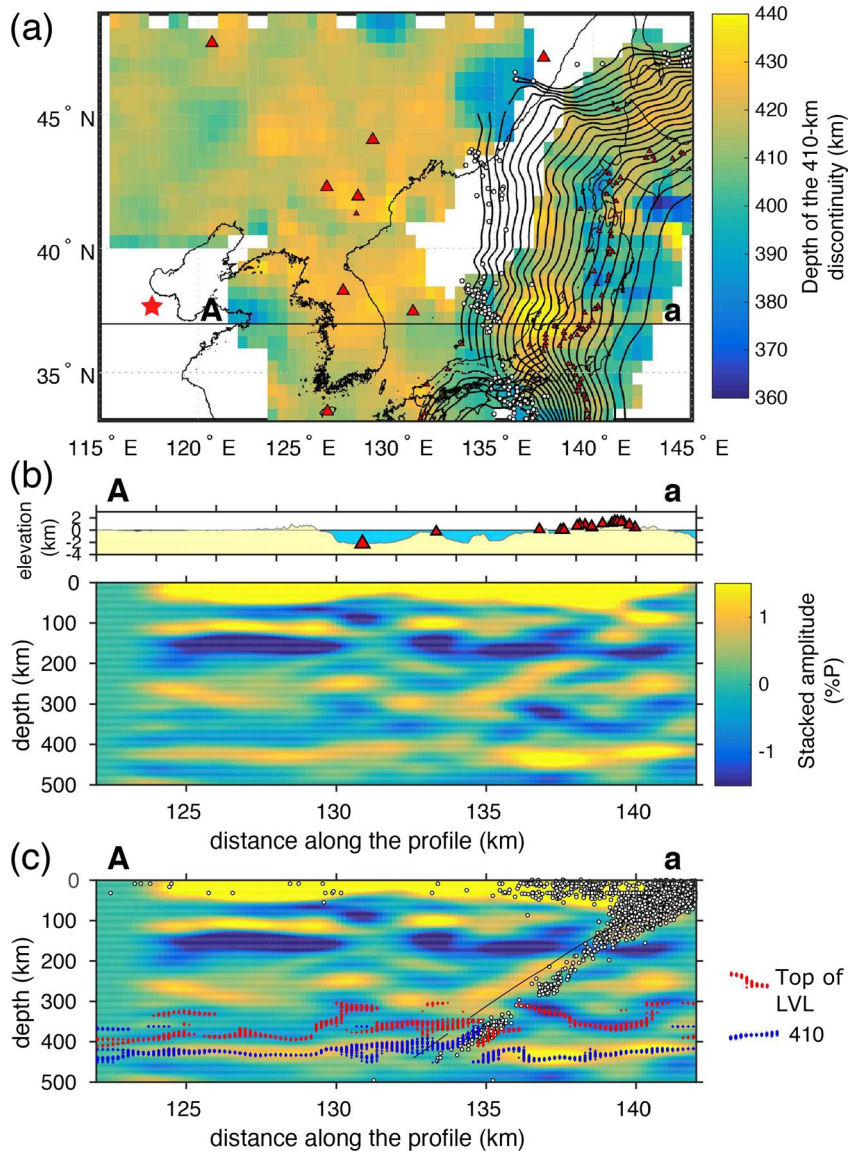

Figure 1. (a) Depth of the top of the mantle transition zone (MTZ) beneath northeast Asia. (b) Vertical cross section of the Ps stacked amplitude along the line marked as A-a in panel (a), and (c) cross section of the amplitude with earthquake locations marked in circles, and the top of the LVL and the MTZ shown in red and blue, respectively. The red star marks the location of Wudi lavas in eastern China (Qian et al., 2020). Small and larger red triangles represent arc-related and intra-plate volcanoes, respectively. Earthquake locations (white dots) are from the USGS catalog, and the plate contour (black line) is from Hayes et al. (2018).

Table 1
Key Seismic Parameters From the Subset of Data Used in This Study

Observed quantities	Median ± 1σ	Range
LVL thickness	61 ± 15 km	15–113 km
MTZ thickness	255 ± 14 km	200–288 km
R_{norm}	−0.68 ± 0.28	−1.83 to −0.18

Note. The original, larger data set is presented by Tauzin et al. (2017). The data in this table is filtered from the larger data set as described in Section 2.1.

selection procedure reduces the initial grid containing 1,490 data points to a grid of 597 data points. In Table 1, we list the values of the key seismic parameters obtained from these 597 data points.

2.2. Rock Physics Analysis

In the rock physics analysis, we separate the seismic signature arising from temperature and bulk composition of the solid from the observed seismic signature. Any residual negative seismic anomaly is then considered to arise from the presence of melt. We calculate the melt volume fraction from this residual seismic anomaly over a large range of input

parameters, which allows us to constrain the uncertainties in the calculated melt volume fraction. We use the open source software MuMaP (Hier-Majumder et al., 2014) to analyze the seismic signals. Details of this method are described by Hier-Majumder et al. (2014) and outlined in the supplementary section.

The first step in the analysis involves calculating a reference shear wave velocity as a function of temperature and solid composition. We convert the seismically determined MTZ thickness at each grid location, using an assumed value for the olivine to wadsleyite Clapeyron slope, γ, to calculate the temperature anomaly at that location using the method suggested by Tauzin and Ricard (2014). Subsequently at each of the grid points, we extrapolate the temperature, T, at MTZ depth from a potential temperature, T_0, at the Earth's surface with a geothermal gradient of 0.3 K/km. Next, assuming a bulk mantle composition, X, described as percentage of basaltic component in the solid, combined with the temperature, we use the database of W. Xu et al. (2008) to evaluate the reference shear wave velocity, $V_S^{ref}(X,T_0,\gamma)$, at each grid point. Notice that the bulk basalt fraction in the mantle can also be expressed as the fraction of recycled slab, f. The relation between these two quantities are discussed in the Supporting Information S1.

Next, we use the normalized amplitude of P-to-S conversion, R_{norm}, to calculate an observed shear wave velocity, V_S^{obs} (Hier-Majumder et al., 2014, Section 2.1.1). We define the normalized residual shear wave velocity anomaly as:

$$\Delta V_S = \frac{V_S^{obs} - V_S^{ref}(X,T_0,\gamma)}{V_S^{ref}(X,T_0,\gamma)}. \tag{1}$$

Since the influences of bulk solid composition and temperature are already accounted for in evaluating ΔV_S, we ascribe any remaining negative values to partial melt. The calculated melt volume fraction can also be influenced by solid-melt dihedral angle (Hier-Majumder & Abbott, 2010; Hier-Majumder et al., 2014). Low dihedral angle melts wet a larger portion of the grain-grain contact, reducing the effective shear modulus of the aggregate and trading off with the absolute melt volume fraction. To account for this trade-off, we use a microstructural model of effective shear wave velocity in a porous medium, which relates the observed and reference shear wave velocities by (Hier-Majumder et al., 2014)

$$V_S^{obs} = \xi(\theta,\phi)V_S^{ref}(X,T_0,\gamma), \tag{2}$$

where the melting anomaly function, $\xi(\theta,\phi)$, depends on both the dihedral angle (θ) and the melt volume fraction (ϕ). Combining Equations 1 and 2, we can also use the alternative expression for the residual shear wave velocity anomaly as

$$\Delta V_S = \xi(\theta,\phi) - 1. \tag{3}$$

We solve the nonlinear, implicit Equation 2 at each grid point for assumed values of potential temperature, T_0, bulk solid composition, X, the Clapeyron slope of olivine to wadsleyite transition, γ, and the dihedral angle θ. Each of these assumed values introduce uncertainties in the final result. We calculate the uncertainty in the melt volume fraction by propagating the error in terms of the uncertainties of these parameters. The complete description of the error estimation for the rock physics analysis can be found in Section 2 of the Supporting Information S1. To evaluate the error from a large parameter space, we use seven values of θ ranging between 10^o and 40^o, nine values of γ ranging from 0.5 to 4.5 MPa/K, nine values of X ranging from 10% to 90%, and five values of T_0, ranging between 1400 and 1800 K to invert the P-S conversion amplitude for each grid location. This range of parameter space resulted in 2,835 separate inversions for each of the 597 grid locations, totaling to nearly 1.7 million inversions.

2.3. Results From the Rock Physics Inversion

Analysis of the filtered subset of seismic data used in this study reveals the presence of a thin, patchy LVL above the MTZ beneath northeast Asia. The LVL is characterized by a negative amplitude of the Ps conversion, a median thickness 61 ± 15 km, and a minimum thickness of 15 km. Combining the MTZ thickness (255 ± 14 km) with the geotherm prescribed by Courtier et al. (2007), we infer a mantle potential temperature of 1535 ± 37 K.

Our analysis reveals the presence of pervasive negative shear wave anomalies in the northeast Asian LVL. While we carried out an extensive number of inversions, here we show a representative analysis of the melt volume fraction. This analysis is carried out for a potential temperature of 1500 K, a dihedral angle of 25^o,

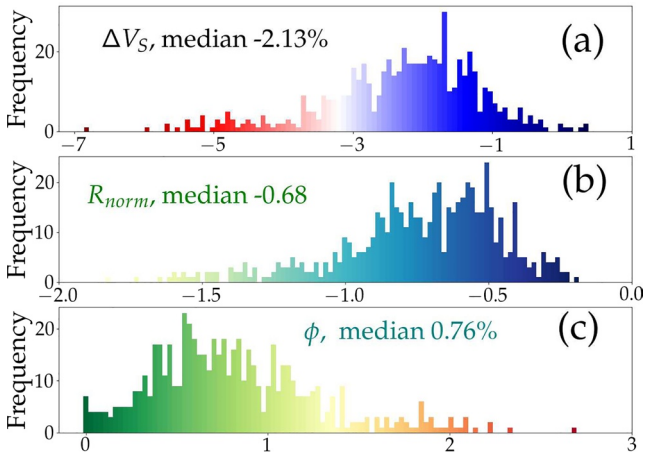

Figure 2. Histograms of seismic data from northeast Asia. (a) Residual shear velocity anomaly, ΔV_S, (b) normalized amplitude of the low velocity layer (LVL) signal, R_{norm}, and (c) melt vol%. Median values of each of these distributions are shown in the text. These distributions were derived from an inversion with a potential temperature of 1500 K, in a mantle containing 27% recycled slab component (40% basalt in the bulk), Clapeyron slope of 3 MPa/K, and a dihedral angle of 25°. Geographical distribution of this data set is mapped in the Supporting Information S1.

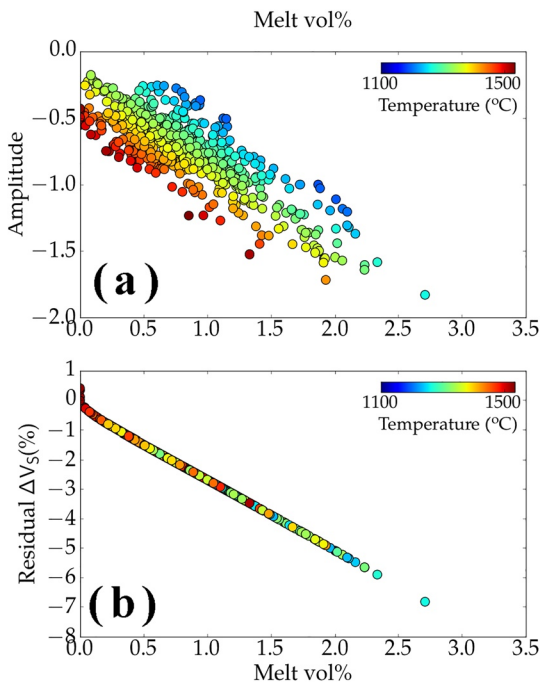

Figure 3. Correlation between (a) amplitude of Ps conversions and (b) residual shear wave anomaly as a function of calculated melt volume fraction. The data points are colored by the temperature independently calculated from the mantle transition zone (MTZ) thickness.

an LVL consisting of 27% recycled slab eclogite (basalt fraction $X = 0.4$), and a Clapeyron slope of 3 MPa/K. As shown in Figure 2a, the residual shear wave velocity anomaly, compensated for the effect of temperature and composition, is largely negative in this region, with percentage values ranging between −6.83 and 0.41. Despite the presence of a few highly negative signals, the median value of $\Delta V_S(\%)$ is −2.13 with a standard deviation of 1.11. This largely negative shear velocity anomaly, not surprisingly, arises from the negative amplitudes of the Ps conversion. The normalized amplitude, R_{norm} is entirely negative in our filtered data set, ranging between dimensionless values of −1.83 and −0.18, with a median of −0.68 (Figure 2b).

The key outcome of our analysis is the detection of pervasive low-degree melting in the northeast Asian LVL. The histogram in Figure 2c outlines the frequency distribution of the melt volume fraction. The median value corrected from the effect of temperature is 0.76 vol% with a propagated uncertainty of 0.53 vol%. Within the LVL, the calculated melt volume fraction varies between 0 and 2.71 vol%. The influence of uncertainties in temperature, dihedral angle, Clapeyron slope, and bulk solid composition are considered in evaluating the uncertainty in the reported melt volume fraction. Here, we only discuss the robustness of our results with respect to temperature in the main text, while the trade-offs between the calculated melt volume fraction and each of these parameters are also shown in the Supporting Information S1 and Hier-Majumder et al. (2014).

Both temperature and melt reduce the effective shear wave velocity, thus rendering the separation of any related effects difficult. In other words, a warmer LVL, characterized by a warmer potential temperature, will register a lower melt volume fraction due to this trade-off. In addition, spatial variations in temperature, calculated from a fixed potential temperature and MTZ thickness, also contribute to this trade-off. For example, the LVL temperature in the data in Figure 2, corresponding to a mantle potential temperature of 1500 K (1223 °C), varied between 1189 and 1534 °C. We quantify the magnitude of this trade-off by the variation in the median melt volume fraction (ϕ) as a function of prescribed mantle potential temperature (T_0). Our error analysis reveals that this variation, $\partial\phi/\partial T_0$ is $-3.2 \times 10^{-5} K^{-1}$. In other words, over or underestimation of the mantle potential temperature by 100 K will under or overestimate the melt by 0.3 vol%. Due to the lack of knowledge of this value, it has been traditionally difficult to quantify the melt volume fraction from seismic interpretations. Our technique of incorporating temperature in the reference shear wave velocity alleviates this problem.

The plots in Figure 3 demonstrate that our method successfully removes the effect of temperature. In Figure 3a, we plot the normalized amplitude of Ps conversion, R_{norm}, from the seismic observations as a function of calculated melt vol%. The data points are colored by the temperature at each grid point. For a given value of the amplitude, warmer data points register lower melt volume fractions, due to the trade-off discussed above. Figure 3b shows the residual $\Delta V_S(\%)$ as a function of the calculated melt volume fraction. Notice that scatter in the data is absent in this plot, as the variations in temperature are already accounted for. Thus, using the temperature and composition compensated residual ΔV_S from Equation 1 to calculate the melt fraction allows us to isolate the effect of melting and calculate the melt volume fraction in a robust manner.

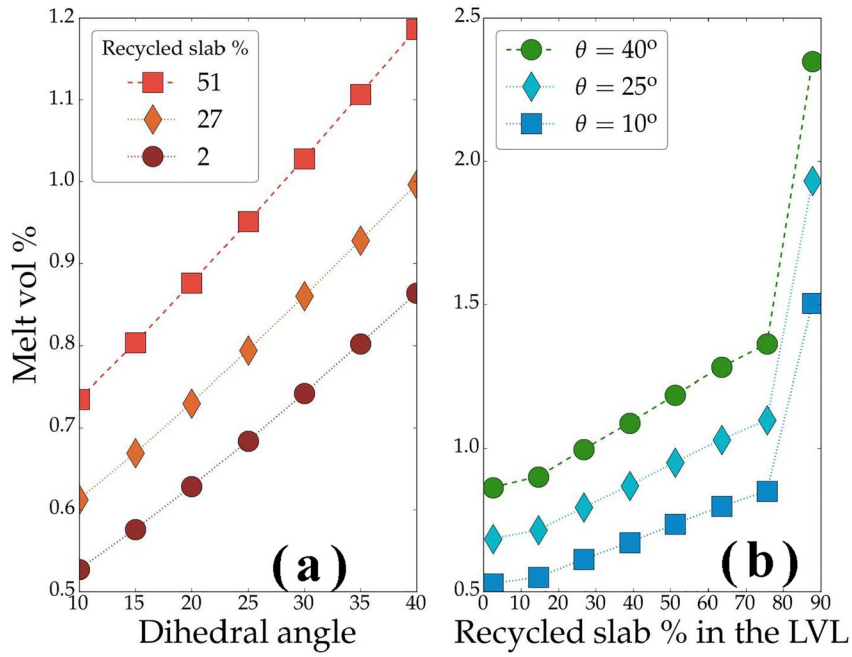

Figure 4. (a) Calculated melt vol% as a function of dihedral angle. The three data sets correspond to three different values of recycled slab component in the bulk low velocity layer (LVL) matrix. (b) Calculated melt vol% as a function of the recycled slab component in the LVL matrix. The legends indicate three different values of dihedral angle. The sudden increase in melt vol% for a recycled slab component of 90% arises from a phase transition in the solid composition (W. Xu et al., 2008), increasing the shear modulus of the solid. As a result, more melt is needed to explain the residual shear velocity anomaly.

In addition to the effect of temperature, we investigate which average melt fraction is supported by varying the seismic data, the dihedral angle and the bulk solid composition on the calculated melt volume fractions, as shown in Figures 4a and 4b. As noticed in the previous similar analyses (Hier-Majumder & Courtier, 2011; Hier-Majumder & Tauzin, 2017; Hier-Majumder et al., 2014; Xiao et al., 2020), for a given potential temperature and bulk solid composition, the predicted melt volume fraction increases with an increase in the solid-melt dihedral angle. Lower dihedral angle melts wet a larger fraction of intergranular contact, reducing the strength of the skeletal mineral framework (Hier-Majumder & Abbott, 2010). As a result, smaller volume fractions of melt are required to explain the reduction in matrix strength depicted by the reduction in shear wave velocity. In turn, the effect of a recycled slab component in the bulk composition, reflected by the bulk basalt fraction, is opposite. A solid consisting of a larger eclogitic slab component is stronger, hence more melt is needed to explain an observed seismic anomaly. In this work, we use a conservative estimate of 27% recycled slab component (40% basalt in the bulk) in the solid. In reality, the LVL above a stalled slab can contain a larger eclogite fraction and register a higher melt volume (Long et al., 2019; Motoki & Ballmer, 2015).

On the basis of the above predictions of melt fraction of each $0.5^{o} \times 0.5^{o}$ cell, we estimate the area of the LVL beneath northeast Asia by integrating the surface area of the cells which have a positive melt fraction. Our estimation shows that the northeast Asian LVL spans over an area of 3.4×10^{6} km^{2}, which is almost twice of the size of the western US LVL, 1.8×10^{6} km^{2} reported by Hier-Majumder and Tauzin (2017). This result is possibly caused by differences in the age of the onset of the subduction and the size of the stagnant slab in the transition zone (Fukao et al., 2009). Long-term stable subduction provides a continuous supply of volatile components for the LVL, while the slab stalled in the transition zone contributes to devolatilization of the subducted slab and LVL generation (Hier-Majumder & Tauzin, 2017; Thomson, Walter, et al., 2016).

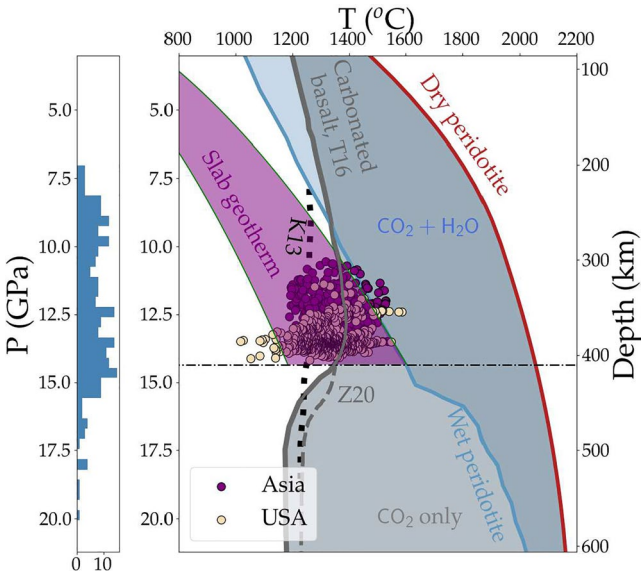

Figure 5. Melting curves of carbonated basalt (Kiseeva et al., 2013; Thomson, Walter, et al., 2016; Zhang et al., 2020), wet peridotite (Ohtani et al., 2004), and dry peridotite (Hier-Majumder & Hirschmann, 2017), overlain by the slab geotherm (Turcotte & Schubert, 2002, Ch. 4). The scatter plot is from temperature and height of the top of the low velocity layers (LVLs) in northeast Asia and the western US. The histogram of the formation pressure of majoritic garnet inclusions in diamond, determined by the barometer of Thomson et al. (2021), is shown on the left panel. The solid gray curve marked "T16" is the solidus of carbonated average MORB with 2.5% CO_2 from Thomson, Walter, et al. (2016). The broken curve, marked "Z20," is the solidus of basalt with 2.5 wt% CO_2 from Zhang et al. (2020). The broken black curve, marked "K13" is a solidus of an altered oceanic crust containing 10 wt% $CaCO_3$, which lost some siliceous component to subarc volcanism from Kiseeva et al. (2013).

3. Volatile Assisted Melting

Although the rock physics analysis predicts the presence of small degree of melting within the LVL, we are unable to constrain the composition of the melt from this analysis. The seismically observed depth and inferred temperature of the LVL, however, provides us with constraints on the nature of melting. Here, we combine the data for the northeast Asian LVL from this study with the previously analyzed data for the western US from Hier-Majumder and Tauzin (2017). As illustrated in Figure 5, converted temperatures and depths to the tops of the LVLs are compared to experimentally determined melting curves for carbonated basalt (Kiseeva et al., 2013; Thomson, Walter, et al., 2016; Zhang et al., 2020), hydrated peridotite (Ohtani et al., 2004), and dry peridotite (Hier-Majumder & Hirschmann, 2017). This comparison is built on two entirely independent sets of constraints, since the rock physics analysis in this work or Hier-Majumder and Tauzin (2017) did not use any constraints from these experimentally determined solidi to infer melt fractions.

Comparison between the seismic data and the experimentally determined solidi suggests that volatiles play a crucial role in melting the LVL mantle. The temperatures in both regions are considerably lower than the dry peridotite solidus and straddle the melting curves of volatile-rich solidi, especially that of carbonated basalts. This result supports the idea of small degree melting above the subducted slabs, aided by the presence of CO_2 and possibly H_2O-rich fluids.

Supporting the role of carbonate-rich melting from the slab are Ti-rich $CaSiO_3$ and majoritic garnet inclusions in sublithospheric diamonds. These inclusions are predominantly of an "eclogitic" or "pyroxenitic" paragenesis, generally marked by enriched trace element abundances indicative of equilibration with a low-degree melt, and are derived from pressures consistent with the low-temperature carbonated eclogite solidus, as shown in the histogram on Figure 5 (Thomson, Walter, et al., 2016; Thomson et al., 2021; Walter et al., 2008). The overlap between the part of the high-pressure peak in the histogram and the LVL suggests that some of these garnets may have formed by reaction between slab-derived, carbonate-rich melts and the LVL mantle.

The reducing ambient mantle predicts that carbonate-rich melts in the LVLs are likely unstable in the peridotite mantle due to the solidi of carbonated peridotite (Brey et al., 2008; Dasgupta et al., 2013; Foley et al., 2009) and redox freezing (Rohrbach & Schmidt, 2011; Sun & Dasgupta, 2019). However, these studies do not consider the rate of solidification. To reconcile this apparent contradiction, our numerical model of reactive porous flow in Sun, Hier-Majumder, et al. (2020) and this study considers the efficiency of redox freezing and the stability of carbonate-rich melts in the reduced mantle. As demonstrated by Sun, Hier-Majumder, et al. (2020), carbonate-rich melts in the LVL can potentially survive redox freezing over long geological time scales (up to hundreds of Ma).

4. Melt Migration Modeling

We model the percolation rate of the buoyant, carbonate-rich melt through the mantle peridotite using a reactive porous flow model (Sun, Hier-Majumder, et al., 2020; Sun, Payton, et al., 2020). Previous numerical simulations of the LVL (Leahy & Bercovici, 2007, 2010) treated the LVL as a homogeneous fluid surrounded by a high viscosity medium, with reactive infiltration driven by a phase change reaction. We now know that the partial melt in the LVL is rather small (0.8 ± 0.5 vol%) and the LVL is a multiphase layer, so our model considers a process of reactive porous flow. To match the theory of "redox freezing" (Rohrbach & Schmidt, 2011), the reaction in this study is the redox reaction between the melt and the mantle matrix, rather than the phase change reaction. In this section, we primarily focus on the influence of the chemical

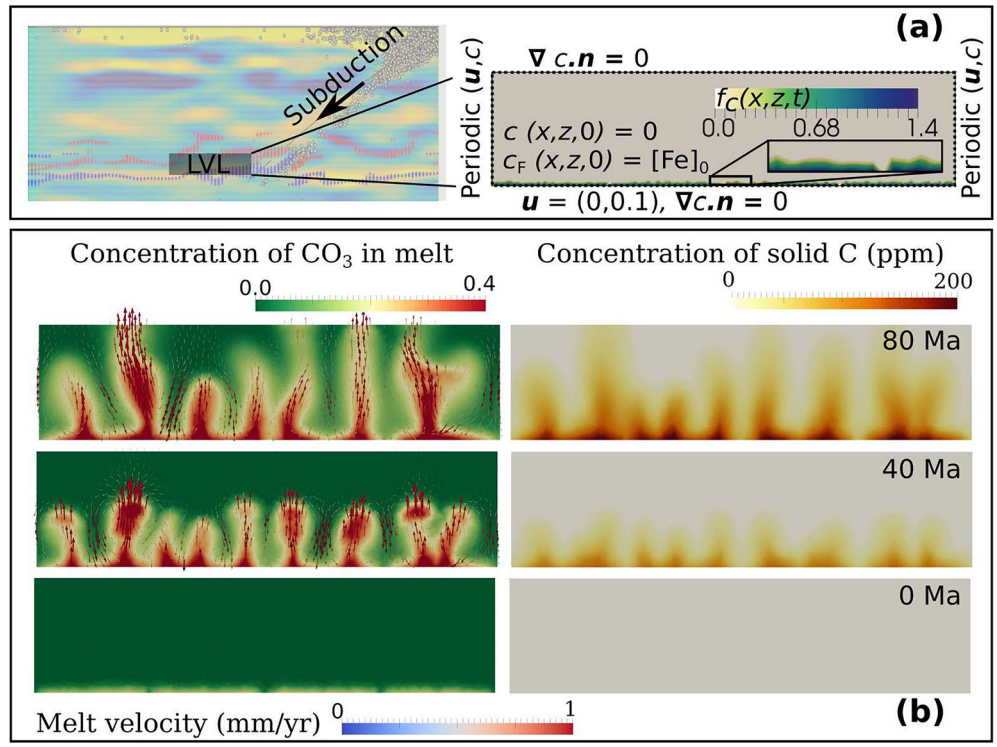

Figure 6. Reactive infiltration instability of carbonate-rich melt channels within the LVL. (a) Model set-up. The figure on the left shows the 2D model of the LVL above the MTZ as a shaded box. The diagram to the right outlines the set-up, initial conditions, and boundary conditions of melt velocity $\boldsymbol{u}$, the concentration (by weight) of the $MgCO_3$ component dissolved in the melt, c, the concentration of Fe in the mantle, c_F, and the spatial distribution of melt input at the bottom of the LVL, f_c. See the text and Sun, Payton, et al. (2020) for more details on the numerical model. (b) Results of numerical simulations. The series of figures on the left depict evolution of the concentration (by weight) of the $MgCO_3$ component dissolved in the melt with the arrows representing the melt velocity. The panels on the right display the concentration of solid carbon in the LVL as a result of reaction between the carbonate melt and the mantle. These simulations were carried out for nondimensional numbers $\mathcal{P}e = 100$, $\mathcal{D}a = 10$, and $\beta = 2$, with an initial Fe concentration of 1 wt% in the mantle.

reaction rate and of the slab-derived carbonate component input rate on the flux of the carbonate component in the melt and the concentration of solid C precipitation. A brief description of the model set-up and the key results are provided in the following two subsections, while details of the model including the dimensional parameters are presented in the Supporting Information S1.

4.1. Numerical Model

In our model, we focus on the LVL above a stalled slab as shown in Figure 6a. Since the carbonate-rich melt released by the subducting slab will be carried by the convective mantle, the mantle of the LVL with the melt will move as a whole horizontally, especially above the stalled slab in the MTZ. However, more important for this study is the vertical migration of the melt and the volatile within the melt, which is driven by porous flow. Under these considerations and assumptions, our model is simplified as slab-derived carbonate-rich melts percolating through a stationary mantle. During its ascent, the metastable carbonate-rich melt reacts with the reduced mantle, leading to the precipitation of solid carbon or carbonate. The freezing of carbonate-rich melts in the ambient mantle can involve two possible mechanisms: carbonation freezing and redox freezing. During carbonation freezing, carbonate-rich melts react with silicates in the mantle to produce carbonate minerals (Sun & Dasgupta, 2019), while redox freezing of carbonate-rich melts lead to the crystallization of solid diamond and metal oxides (Rohrbach & Schmidt, 2011). Carbonation freezing depends on slab-surface temperature-pressure conditions, local volatile influx, and the infiltrating melt composition. Redox freezing, in turn, is controlled by the reducing conditions in the ambient mantle. While

both types of reaction are plausible, the numerical model of reactive infiltration in this article focuses on the redox freezing reaction, which is better characterized and evidenced more widely by superdeep diamonds. In future studies, the role of carbonation freezing can be modeled using the same theoretical construct presented in this section. While a number of plausible chemical reactions can be used to describe redox freezing, we consider the following reaction between the dissolved carbonate component in the melt and free Fe in the mantle (Dorfman et al., 2018; Rohrbach & Schmidt, 2011),

$$MgCO_3(\text{melt}) + 2Fe(\text{solid}) = 3Fe_{2/3}Mg_{1/3}O(\text{solid}) + C(\text{solid}). \tag{4}$$

This chemical reaction is strongly coupled to the reactive porous flow of the melt, described by a set of partial differential equations. We solve this system of five governing equations for five variables; the concentration of the carbonate component in the melt (c), the concentrations of solid Fe and C in the mantle (c_F and c_C, respectively), the percolation velocity of the melt ($\boldsymbol{u}$), and the fluid pressure (p). The nondimensional form of governing equations is given by,

$$\phi \boldsymbol{u} = -\left(\nabla p - \left(1 + c\right)\hat{\boldsymbol{z}}\right), \tag{5}$$

$$\nabla \cdot \boldsymbol{u} = 0, \tag{6}$$

$$\frac{\partial c}{\partial t} + \boldsymbol{u} \cdot \nabla c = \frac{1}{\mathcal{P}e}\nabla^2 c - \frac{\mathcal{D}a\,\alpha}{\phi}\, c c_F^2 + \beta f_c, \tag{7}$$

$$\frac{\partial c_F}{\partial t} = -\frac{\mathcal{D}a\,\alpha_F}{1-\phi}\, c c_F^2, \tag{8}$$

$$\frac{\partial c_C}{\partial t} = \frac{\mathcal{D}a\,\alpha_C}{1-\phi}\, c c_F^2, \tag{9}$$

where t is time and f_c is the dimensionless rate of carbonate influx to the mantle. The constants $\alpha_i = n_i(M_i/\Sigma_i M_i)$ are products of the stoichiometric coefficients, n_i of the th component (carbonate in melt, Fe and C in the mantle) and the molecular weight fractions, $(M_i/\Sigma_i M_i)$, in Equation 4. This system of equations also contains three dimensionless parameters, the Péclet number ($\mathcal{P}e$), the Damköhler number ($\mathcal{D}a$), and the rate of carbonate influx by subduction, β, defined as,

$$\mathcal{P}e = \frac{u_0 H}{D},\ \mathcal{D}a = \frac{\Gamma_0 H}{u_0},\ \text{and}\ \beta = \frac{f_0 H}{\phi u_0}, \tag{10}$$

where u_0 is the characteristic melt velocity, H is the characteristic thickness of the LVL, D is the chemical diffusivity, ϕ is the average melt fraction, Γ_0 is the rate of chemical reaction, and f_0 is the mass fraction of subducted carbonate per unit time.

The nondimensional numbers indicate the relative rates of the different processes involved in the reactive infiltration instability. The Péclet number, $\mathcal{P}e$, characterizes the ratio between the rates of dissolved carbonate transport by advection and diffusion. The Damköhler number ($\mathcal{D}a$) represents the ratio between the rates of chemical reaction and percolation. In this study, we select a narrower range, similar to that suggested by Spiegelman et al. (2001), and report results for $\mathcal{P}e$ ranging between 10 and 100 and $\mathcal{D}a$ ranging between 1 and 100, while the study of Sun, Payton, et al. (2020) explored a wider range of values of these two parameters. Owing to this choice of a conservative $\mathcal{P}e$ and a relatively high value of $\mathcal{D}a$, our estimated values of carbonate-melt flux into the mantle are likely more conservative than the natural values. Present day of values of the dimensionless carbonate flux per unit time, β, varies from < 1 to ~ 4 along both coasts of the Pacific (Sun, Payton, et al., 2020, also see Supporting Information S1). We carried out simulations for β varying over a range between 0.1 and 6 in this study.

The model set-up and boundary conditions are displayed in the schematic diagram in Figure 6a. We solve the governing equations by adopting a set of Dirichlet, Neumann, and periodic boundary conditions on the primary unknowns, $\boldsymbol{u}$ and c. The complete set of boundary conditions are given by,

$$\boldsymbol{u} = w_0\,\hat{\boldsymbol{z}} \text{ on } \partial\Omega_b, \tag{11}$$

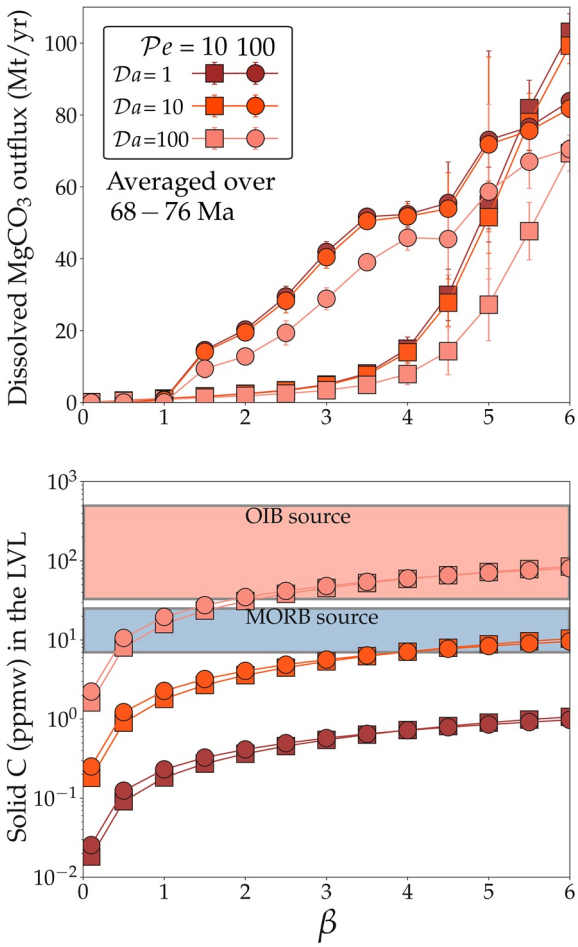

Figure 7. (a) Flux of dissolved carbonate component in the melt through the top of the northeast Asian low velocity layer (LVL). The values are averaged over a time period shown in the inset. The error bars indicate the standard deviation over the same time range. (b) Concentration of solid carbon in the LVL as a function of β, the dimensionless carbonate input rate to the LVL. For reference, we also show the total (molten and solid) carbon concentrations in the OIB and MORB sources (Hirschmann & Dasgupta, 2009). Error bars in this plot are smaller than the symbol sizes.

$$\boldsymbol{u}, c \quad = \quad \text{periodic on } \partial\Omega_v, \tag{12}$$

$$\nabla c \cdot \hat{\boldsymbol{n}} \quad = \quad 0 \text{ on } \partial\Omega_N, \tag{13}$$

where $w_0 = 0.1$ is the dimensionless prescribed melt velocity at the bottom boundary, $\partial\Omega_b$. Using a characteristic melt velocity of $u_0 = 1$ mm/yr, this boundary condition represents a dimensional boundary melt velocity of 100 μm/yr, similar to the estimates by Hier-Majumder and Tauzin (2017). We use a free boundary at the top, $\partial\Omega_t$, and impose periodic boundaries in both $\boldsymbol{u}$ and c along the vertical walls of the domain, $\partial\Omega_v$. Finally, we set a zero diffusive flux Neumann condition on c at the top and bottom boundaries, $\partial\Omega_N = \partial\Omega_b \bigcup \partial\Omega_t$.

Since this is a time-dependent problem, the necessary initial conditions are prescribed as zero carbonate in the melt, 1 wt% free Fe and zero solid carbon in the mantle prior to the onset of melt percolation, namely,

$$c(x,z,0) = 0, c_F(x,z,0) = \left[\text{Fe}\right]_0, \text{and } c_C = 0, \tag{14}$$

where $[\text{Fe}]_0 = 0.01$ is the metallic iron mass fraction in the mantle matrix.

We discretize the governing PDEs using the finite element method. Then, based on the open source code MuPoPP, we generate the mesh, solve the discretized algebraic equations using Krylov sparse solvers, and output the data for further visualization and analysis.

4.2. Melt Channels, Residence Time, and Fluxes

The series of visualizations in Figure 6 display three snapshots in time, spanning over 80 Ma, demonstrating that carbonate-rich melts can survive redox freezing. Under these conditions ($\mathcal{P}e = 100, \mathcal{D}a = 10, \beta = 2$), melt migration occurs through localized channels. Channelization also leads to the formation of reaction zones containing up to 200 parts per million by weight (ppmw) solid carbon (Figure 6, right), marking the sites of diamond formation. Mantle-derived melts arising from the LVLs can thus inherit geochemical components from the reaction zone and the nonreactive parts of the mantle, indicating heterogeneous geochemical signatures of their sources, as sometimes observed in basalts from northeast Asia (Qian et al., 2020; S. Li et al., 2017).

The flux of the carbonate component in the melt and the concentration of solid C, mapped over the parameter space in Figure 7, provide important information about carbon storage in the LVL. First, the flux of the carbonate component in the melt is strongly dependent on the carbonate input from subduction, as shown by the plot in Figure 7a. While this result is physically intuitive, it contradicts the conclusion that redox freezing completely consumes carbonate-rich melts (Rohrbach & Schmidt, 2011). To fully understand the stability of these melts, the rate of input from subduction must also be taken into account. We calculated the dimensional value of the flux using the calculated value of the northeast Asian LVL surface area, approximately 3.4×10^6 km^2. This calculation shows that an LVL of the size of the northeast Asian LVL can transfer up to 100 Mt/yr of dissolved carbonate component to the upper mantle, namely 52 Mt/yr of CO_2. Second, this plot also demonstrates that the control of subduction input on the flux is substantially modified by the $\mathcal{P}e$ number. While the dependence is nearly linear for $\mathcal{P}e = 100$, the flux remains much lower for $\mathcal{P}e = 10$ when $\beta < 4$. Third, the influence of melt reactivity, characterized by the $\mathcal{D}a$ number, is more pronounced on the concentration of average solid carbon concentration than the flux of melt carbonate, as revealed by a comparison between Figures 7a and 7b. With a tenfold increase in $\mathcal{D}a$, the C concentration in ppmw in the mantle also increases by nearly an order of magnitude. Over the range of parameters shown in the plot, the LVL sequesters between 0.1 and 80 ppmw solid C on average, while the LVL can locally

sequester up to 200 ppmw solid C (Figure 6b). Finally, the solid C concentration in the LVL increases with an increase in the subducted carbonate input. This result outlines the fact that the accumulation of solid C in the mantle might have varied over time, as the rate of subduction and the amount of slab-derived carbon varied.

An important outcome of the numerical models is the relatively sluggish velocity of melt percolation. The simulations in Figure 6 show that the melt channels reach the top of a 40 km thick LVL in 80 Ma, at a velocity of 0.5 km/Ma (500 μm/yr). This velocity is even lower, ~0.2 km/Ma (200 μm/yr), when the melt propagation takes place through a planar front (see the Supplementary Material), implying that the melt can take between 200 and 500 Ma to reach the top of the thickest parts of the LVL (113 km, Table 1). These estimates of sluggish melt flow bear two important consequences. First, the relatively immobile slab-derived melt can be entrained into faster moving upwelling convective flow and transported to shallower levels. Second, the several hundred million years of the melt residence time will allow extensive mantle metasomatism and in-growth of isotopic animalies.

5. Geochemistry

Inclusions in diamonds and petrological modeling provide evidence for the kinds of melts that may exist above a subducted slab in the transition zone, leading to metasomatism of mantle peridotite and generation of geochemically distinct sources. Inclusions of $Ca(Ti,Si)O_3$ in diamond, interpreted as former Ca-perovskite, and many majoritic garnets have major and trace element compositions indicating derivation from subducted oceanic crust (Bulanova et al., 2010; Thomson et al., 2014; Thomson, Kohn, et al., 2016; Walter et al., 2008). In particular, extreme enrichments in many incompatible elements (e.g., Th, U, Nb, Ta, REE) are inconsistent with a subsolidus origin from basaltic crust, but are best modeled by equilibration with a low-degree melt, likely of carbonatitic affinity, derived from subducted eclogitic crust in the transition zone (Bulanova et al., 2010; Thomson, Kohn, et al., 2016; Thomson, Walter, et al., 2016; Walter et al., 2008). Further support for an origin in or close to the transition zone is a major peak in the crystallization pressures at ~14 GPa in the global database of majoritic garnet inclusions of eclogitic affinity (Thomson et al., 2021), in good agreement with estimates of the pressure at which slab top geotherms are expected to cross the solidus of carbonated eclogite shown in Figure 5 (Kiseeva et al., 2013; Walter et al., 2008; Zhang et al., 2020).

To illustrate the result of such interactions between a carbonate-rich melt and the mantle, Figure 8a shows the composition of a $Ca(Ti,Si)O_3$ inclusion from Juina, Brazil (J1) (dashed green line) that has been identified as crystallizing from a primitive melt of oceanic crust (Bulanova et al., 2010; Walter et al., 2008). Also shown is the estimated trace element composition of the coexisting melt (solid green line) on the basis of experimental partitioning coefficients, where $C_{melt} = C_{min}/D^{min/melt}$ and using partition coefficients from Thomson, Kohn, et al. (2016). The red dashed line represents a model of subducted, processed oceanic crust where a total of 10% hydrous component has been extracted at 2.5, 4.5, and 6 GPa, mimicking crust dehydration and using experimentally derived mineral/fluid partition coefficients (Kessel et al., 2005; Klimm et al., 2008; Thomson, Kohn, et al., 2016). Dehydration mobilizes elements like Sr and Pb relative to other trace elements. The solid red line represents a low-degree melt (0.1%) of processed MORB at transition zone conditions calculated using the methods, partition coefficients, and melting reactions described by Thomson, Kohn, et al. (2016). Also shown is a shaded field of calculated melts that could coexist with clinopyroxene xenocrysts from the Cenozoic Wudi basalt from eastern China (Qian et al., 2020). We note the striking similarity in the overall abundance patterns, and especially the Sr, Pb, Hf, and Zr depletions, as well as the predicted high U/Pb and Th/Pb ratios of all of these independently estimated melt compositions that potentially represent slab-derived melts present in the LVL above a subducted slab at transition zone depths. The black line shows the trace element abundances expected in primitive peridotitic mantle after the addition of 1% of the model low-degree melt derived from the subducted processed oceanic crust.

Figure 8b shows the modeled Pb isotopic evolution of the metasomatized mantle by addition of 1% of the low-degree melt produced from processed MORB for time periods of 100, 500, and 1,000 Ma. Also shown are the Pb isotopic compositions of clinopyroxene xenocrysts in Wudi lavas that have recorded equilibration with a HIMU like melt beneath eastern China (Qian et al., 2020). Although these results are model dependent and

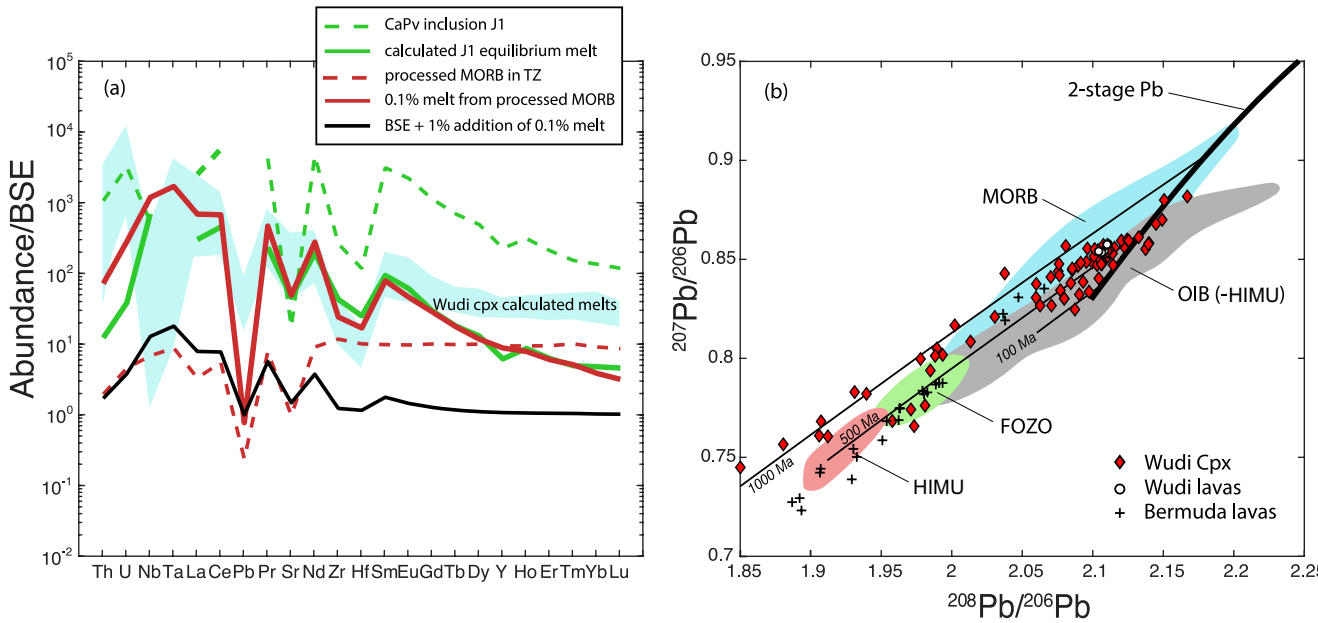

Figure 8. (a) Trace element abundances normalized to bulk silicate Earth (BSE) (McDonough & Sun, 1995) showing model compositions of low-degree carbonated melts of oceanic crust in the transition zone. See the text in Section 5 for more details. (b) Plot in $^{208}Pb/^{206}Pb$ versus $^{207}Pb/^{206}Pb$ isotopic space showing fields for mantle derived basalts (MORB, OIB, FOZO HIMU) from Stracke et al. (2005), HIMU lavas from Bermuda (crosses, Mazza et al., 2019), lavas from Wudi, E. China (white circles, Qian et al., 2020) and clinopyroxene xenocrysts from the Wudi lavas (red diamonds, Qian et al., 2020). The thick black line shows a model two-stage growth curve using model parameters from Stacey and Kramers (1975). The thin black lines are growth curves for mantle metasomatized by addition of 1% of the low-degree melt produced from processed MORB, where age labels represent the time of metasomatism.

are not meant to be dispositive, we note that HIMU-type lavas can be generated from the model melt-metasomatized peridotitic source in ~500 Ma. On the basis of isotopic and geochemical constraints, Qian et al. (2020) suggested that melts from dehydrated, carbonated oceanic crust have the chemical characteristics required for the HIMU component recorded in the Wudi xenocrysts, and indicated a mantle source metasomatized by carbonatitic melt from subducted crust no older than 700 Ma, consistent with our modeling. Likewise, high $^{206}Pb/^{204}Pb$ and low $^{207}Pb/^{204}Pb$ lavas from Bermuda have also been suggested to be caused by deep mantle metasomatism from a volatile-rich melt no earlier than ~500 Ma ago (Mazza et al., 2019), again consistent with our modeling of metasomatized mantle by carbonated melts derived from subducted oceanic crust. We note that calculated values at 500 Ma for $^{87}Sr/^{86}Sr$ (~ 0.7030), $^{143}Nd/^{144}Nd$ (~ 0.5130) and $^{176}Hf/^{177}Hf$ (~0.2829) using our model parameters are also generally consistent with a HIMU-like mantle source (Stracke et al., 2005). Overall, our modeling indicates that deep metasomatism of the mantle through the interaction with melts derived from oceanic crust is a viable mechanism to produce a HIMU-like component in eastern China Wudi lavas and likely anywhere that deep subduction results in melting of carbonated oceanic crust (Castillo, 2015; Weiss et al., 2016; Y. Xu et al., 2012; H. Li et al., 2016).

6. Discussions and Conclusions

Our rock physics analysis of the Ps conversion data indicates that the northeast Asian LVL is marked by an average of 0.8 vol% melt, with occasional patches exceeding > 2 vol% melt (Figure 2). Comparison of the inferred temperature and depth of the seismic data from this study and a similar study of the LVL beneath the western US reveals, independently, that the melting is assisted by CO_2 and/or H_2O (Figure 5), suggesting the LVLs as potential volatile reservoirs in the deep upper mantle. Considering that both the western US and northeast Asia are influenced by subduction with stagnant slabs in the MTZ, volatile-enhanced components that induce partial melting in the LVL can be derived from these subducted slabs. A considerable number of geochemical studies on Cenozoic basalts and inclusions in diamond also support the subducted slab as the transmission band of volatiles from the Earth's surface to the deep upper mantle (Bulanova et al., 2010; S. Li et al., 2017; Qian et al., 2020; Thomson, Kohn, et al., 2016; Thomson, Walter, et al., 2016; Walter et al., 2008).

To compensate the lack of direct samples, we implemented geodynamical and geochemical modeling methods. Our model of reactive porous flow demonstrates that carbonate-rich melts in the LVL migrate slowly, with velocities ranging between 200 and 500 μm/yr, trapping the melt in the LVL for up to 500 Ma. The results also show that an LVL similar to the northeast Asian LVL in areal extent (3.4×10^6 km^2) can transfer up to 52 Mt/yr of CO_2 from the subducting slab to the upper mantle (Figure 7a). As the two most representative LVLs associated with the subduction zones, the LVLs beneath northeast Asia and the western US are estimated to have a total area of 5.2×10^6 km^2 and can transfer up to 78 Mt/yr CO_2 in total. This value of carbon flux through the top of the LVLs is of similar magnitude to the global subducted carbon fluxes between 80–176 Mt/yr (Dasgupta & Hirschmann, 2010) and 300 ± 50 Mt/yr (Plank & Manning, 2019) CO_2, suggesting that the LVLs related to subduction can be significant reservoirs of subducted carbon in the deep upper mantle, and an important component of the global carbon budget. At the same time, as the simulations predict in Figures 6b and 7b, the LVL can immobilize up to 80 ppmw solid C on average to the deep upper mantle by redox freezing, and even up to 200 ppmw solid C distributed in localized reaction zones. Compared to the carbon content of either the OIB source with 120–1,830 ppm CO_2 or the MORB source with 25–95 ppm CO_2 (Hirschmann & Dasgupta, 2009), this process can effectively increase the regional carbon content fixed in the mantle, demonstrating the potential of the LVL as a deep carbon reservoir. These results bear implications for the big mantle wedge (BMW) beneath northeast Asia. For example, the geochemical signature in the source of the Wudi basalts could have resulted from reaction between slab-derived melt and the ambient mantle during an early Cretaceous subduction event, which also led to the formation of the big mantle wedge beneath northeast Asia (Ma & Xu, 2021). The melt residence time in the LVL in our simulations is consistent with the timing of these two events in the northeast Asian upper mantle. Finally, using the estimated melt fractions, our geochemical model calculates the abundances of trace elements resulting from the melt-mantle interaction (Figure 8), demonstrating that such interaction can produce a HIMU like source component. When the HIMU like metasomatized mantle is carried by upwelling convective flow of the upper mantle to the base of the lithosphere, they will sustain the intraplate volcanism and form basalts, which inherit components or geochemical characters of the LVL, like the HIMU component in eastern China Wudi lavas.

While the results of this study, combining several different techniques, bears important implications for the global carbon cycle, a few factors need to be taken into account. First, future seismic investigations, employing a denser array of sensors will greatly improve the resolution of the seismic data and provide a more detailed picture of the internal structure of the LVL. Second, the calculated melt volume fraction depends on a number of assumed parameters. While we carried out a rigorous analysis spanning a large parameter space and reported the uncertainties associated with each of the parameters, future inversions using similar rigorous constraints on different seismic datasets will provide additional constraints on the melt fraction in the LVL. Third, our numerical simulation of melt migration is carried out in a two-dimensional domain, greatly simplifying the complex geometry of the LVL. In addition, these simulations do not account for possible temporal variations in the carbonate flux associated with subduction. Future 3D melt migration simulations, based on the tectonic history of the western Pacific subduction zone, will greatly enhance our understanding of the fluxes and residence times of carbonate-rich melts in the mantle beneath northeast Asia. Finally, such simulations will also aid in understanding the evolution of the geochemical signature of the mantle over time periods longer than those considered in this work.

Data Availability Statement

Seismic and geochemical datasets for this research are available in these in-text data citation references: Tauzin et al. (2017), Bulanova et al. (2010), Thomson et al. (2014), Thomson, Kohn, et al. (2016). The source codes for the melt volume fraction analysis, MuMaP (MUltiphae MAterial Properties), and the melt migration simulation, MuPoPP1.2.0 (Multiphase Porous flow and Physical Properties) are publicly available (respectively at https://doi.org/10.5281/zenodo.3673226 and https://doi.org/10.5281/zenodo.3631108). Simulation data will also be available for download through the Royal Holloway Figshare repository (https://royalholloway.figshare.com/).

Acknowledgments
The authors acknowledge the financial supports from the National Natural Science Foundation of China (41688103) and the Chinese Academy of Sciences (XDB18000000). Y. Z. Sun is supported by a joint PhD program between the Guangzhou Institute of Geochemistry, Chinese Academy of Sciences, and Royal Holloway University of London. B. Tauzin is supported by the European Union's Horizon 2020 Research and Innovation programme under the Marie Sklodowska-Curie grant agreement 793824. The authors thank Dr. Liang Liu for helpful discussions. They also thank two anonymous reviewers, and the Associate Editor, Stephen Parman, for their insightful suggestions and comments.

References

Bagley, B., Courtier, A. M., & Revenaugh, J. (2009). Melting in the deep upper mantle oceanward of the Honshu slab. *Physics of the Earth and Planetary Interiors*, *175*(3–4), 137–144. https://doi.org/10.1016/j.pepi.2009.03.007

Brey, G. P., Bulatov, V. K., Girnis, A. V., & Lahaye, Y. (2008). Experimental melting of carbonated peridotite at 6-10 GPa. *Journal of Petrology*, *49*(4), 797–821. https://doi.org/10.1093/petrology/egn002

Bulanova, G. P., Walter, M. J., Smith, C. B., Kohn, S. C., Armstrong, L. S., Blundy, J., & Gobbo, L. (2010). Mineral inclusions in sublithospheric diamonds from Collier 4 kimberlite pipe, Juina, Brazil: Subducted protoliths, carbonated melts and primary kimberlite magmatism. *Contributions to Mineralogy and Petrology*, *160*(4), 489–510. https://doi.org/10.1007/s00410-010-0490-6

Burnham, A. D., Thomson, A. R., Bulanova, G., Kohn, S. C., Smith, C. B., & Walter, M. J. (2015). Stable isotope evidence for crustal recycling as recorded by superdeep diamonds. *Earth and Planetary Science Letters*, *432*, 374–380. https://doi.org/10.1016/j.epsl.2015.10.023

Castillo, P. R. (2015). The recycling of marine carbonates and sources of HIMU and FOZO ocean island basalts. *Lithos*, *216*, 254–263. https://doi.org/10.1016/j.lithos.2014.12.005

Chevrot, S., Vinnik, L., & Montagner, J.-P. (1999). Global-scale analysis of the mantle Pds phases. *Journal of Geophysical Research*, *104*(B9), 20203–20219. https://doi.org/10.1029/1999JB900087

Courtier, A. M., Jackson, M. G., Lawrence, J. F., Wang, Z., Lee, C.-T. A., Halama, R., et al. (2007). Correlation of seismic and petrologic thermometers suggests deep thermal anomalies beneath hotspots. *Earth and Planetary Science Letters*, *264*(1–2), 308–316. https://doi.org/10.1016/j.epsl.2007.10.003

Courtier, A. M., & Revenaugh, J. (2007). Deep upper-mantle melting beneath the Tasman and Coral Seas detected with multiple ScS reverberations. *Earth and Planetary Science Letters*, *259*(1–2), 66–76. https://doi.org/10.1016/j.epsl.2007.04.027

Dasgupta, R., & Dixon, J. E. (2009). Volatiles and volatile-bearing melts in the Earth's interior. *Chemical Geology*, *262*(1), 1–3. https://doi.org/10.1016/j.chemgeo.2009.04.006

Dasgupta, R., & Hirschmann, M. M. (2010). The deep carbon cycle and melting in Earth's interior. *Earth and Planetary Science Letters*, *298*(1–2), 1–13. https://doi.org/10.1016/j.epsl.2010.06.039

Dasgupta, R., Mallik, A., Tsuno, K., Withers, A. C., Hirth, G., & Hirschmann, M. M. (2013). Carbon-dioxide-rich silicate melt in the Earth's upper mantle. *Nature*, *493*(7431), 211–215. https://doi.org/10.1038/nature11731

Dorfman, S. M., Badro, J., Nabiei, F., Prakapenka, V. B., Cantoni, M., & Gillet, P. (2018). Carbonate stability in the reduced lower mantle. *Earth and Planetary Science Letters*, *489*, 84–91. https://doi.org/10.1016/j.epsl.2018.02.035

Eagar, K. C., Fouch, M. J., & James, D. E. (2010). Receiver function imaging of upper mantle complexity beneath the Pacific Northwest, United States. *Earth and Planetary Science Letters*, *297*(1–2), 141–153. https://doi.org/10.1016/j.epsl.2010.06.015

Fee, D., & Dueker, K. (2004). Mantle transition zone topography and structure beneath the Yellowstone hotspot. *Geophysical Research Letters*, *31*(18). https://doi.org/10.1029/2004GL020636

Foley, S. F., Yaxley, G. M., Rosenthal, A., Buhre, S., Kiseeva, E. S., Rapp, R. P., & Jacob, D. E. (2009). The composition of near-solidus melts of peridotite in the presence of CO_2 and H_2O between 40 and 60kbar. *Lithos*, *112*, 274–283. https://doi.org/10.1016/j.lithos.2009.03.020

Freitas, D., Manthilake, G., Schiavi, F., Chantel, J., Bolfan-Casanova, N., Bouhifd, M. A., & Andrault, D. (2017). Experimental evidence supporting a global melt layer at the base of the Earth's upper mantle. *Nature Communications*, *8*(1), 2186. https://doi.org/10.1038/s41467-017-02275-9

Fukao, Y., Obayashi, M., Nakakuki, T., & Group, D. S. P. (2009). Stagnant slab: A review. *Annual Review of Earth and Planetary Sciences*, *37*, 19–46. https://doi.org/10.1146/annurev.earth.36.031207.124224

Gao, W., Matzel, E., & Grand, S. P. (2006). Upper mantle seismic structure beneath eastern Mexico determined from P and S waveform inversion and its implications. *Journal of Geophysical Research*, *111*(B8). https://doi.org/10.1029/2006JB004304

Gorman, P. J., Kerrick, D., & Connolly, J. (2006). Modeling open system metamorphic decarbonation of subducting slabs. *Geochemistry, Geophysics, Geosystems*, *7*(4), 1–21. https://doi.org/10.1029/2005GC001125

Han, G., Li, J., Guo, G., Mooney, W. D., Karato, S., & Yuen, D. A. (2021). Pervasive low-velocity layer atop the 410-km discontinuity beneath the northwest Pacific subduction zone: Implications for rheology and geodynamics. *Earth and Planetary Science Letters*, *554*, 116642. https://doi.org/10.1016/j.epsl.2020.116642

Harte, B. (2010). Diamond formation in the deep mantle: The record of mineral inclusions and their distribution in relation to mantle dehydration zones. *Mineralogical Magazine*, *74*(2), 189–215. https://doi.org/10.1180/minmag.2010.074.2.189

Hayes, G. P., Moore, G. L., Portner, D. E., Hearne, M., Flamme, H., Furtney, M., & Smoczyk, G. M. (2018). Slab2, a comprehensive subduction zone geometry model. *Science*, *362*(6410), 58–61. https://doi.org/10.1126/science.aat4723

Hier-Majumder, S., & Abbott, M. E. (2010). Influence of dihedral angle on the seismic velocities in partially molten rocks. *Earth and Planetary Science Letters*, *299*(1–2), 23–32. https://doi.org/10.1016/j.epsl.2010.08.007

Hier-Majumder, S., & Courtier, A. (2011). Seismic signature of small melt fraction atop the transition zone. *Earth and Planetary Science Letters*, *308*(3–4), 334–342. https://doi.org/10.1016/j.epsl.2011.05.055

Hier-Majumder, S., & Hirschmann, M. M. (2017). The origin of volatiles in the Earth's mantle. *Geochemistry, Geophysics, Geosystems*, *18*(8), 3078–3092. https://doi.org/10.1002/2017GC006937

Hier-Majumder, S., Keel, E. B., & Courtier, A. M. (2014). The influence of temperature, bulk composition, and melting on the seismic signature of the low-velocity layer above the transition zone. *Journal of Geophysical Research: Solid Earth*, *119*(2), 971–983. https://doi.org/10.1002/2013JB010314

Hier-Majumder, S., & Tauzin, B. (2017). Pervasive upper mantle melting beneath the western US. *Earth and Planetary Science Letters*, *463*, 25–35. https://doi.org/10.1016/j.epsl.2016.12.041

Hirschmann, M. M. (2006). Water, melting, and the deep Earth H_2O cycle. *Annual Review of Earth and Planetary Sciences*, *34*, 629–653. https://doi.org/10.1146/annurev.earth.34.031405.125211

Hirschmann, M. M., & Dasgupta, R. (2009). The H/C ratios of Earth's near-surface and deep reservoirs, and consequences for deep Earth volatile cycles. *Chemical Geology*, *262*(1–2), 4–16. https://doi.org/10.1016/j.chemgeo.2009.02.008

Ickert, R. B., Stachel, T., Stern, R. A., & Harris, J. W. (2015). Extreme ^{18}O-enrichment in majorite constrains a crustal origin of transition zone diamonds. *Geochemical Perspectives Letters*, *1*(1), 65–74. https://doi.org/10.7185/geochemlet.1507

Jasbinsek, J., & Dueker, K. (2007). Ubiquitous low-velocity layer atop the 410-km discontinuity in the northern Rocky Mountains. *Geochemistry, Geophysics, Geosystems*, *8*(10). https://doi.org/10.1029/2007GC001661

Jasbinsek, J., Dueker, K. G., & Hansen, S. M. (2010). Characterizing the 410 km discontinuity low-velocity layer beneath the LA RISTRA array in the North American Southwest. *Geochemistry, Geophysics, Geosystems*, *11*(3). https://doi.org/10.1029/2009GC002836

Kelemen, P. B., & Manning, C. E. (2015). Reevaluating carbon fluxes in subduction zones, what goes down, mostly comes up. *Proceedings of the National Academy of Sciences*, *112*(30), 3997–4006. https://doi.org/10.1073/pnas.1507889112

Kessel, R., Schmidt, M. W., Ulmer, P., & Pettke, T. (2005). Trace element signature of subduction-zone fluids, melts and supercritical liquids at 120-180 km depth. *Nature*, *437*(7059), 724–727. https://doi.org/10.1038/nature03971

Kiseeva, E. S., Litasov, K. D., Yaxley, G. M., Ohtani, E., & Kamenetsky, V. S. (2013). Melting and phase relations of carbonated eclogite at 9-21gpa and the petrogenesis of alkali-rich melts in the deep mantle. *Journal of Petrology*, *54*(8), 1555–1583. https://doi.org/10.1093/petrology/egt023

Klimm, K., Blundy, J. D., & Green, T. H. (2008). Trace element partitioning and accessory phase saturation during H_2O-saturated melting of basalt with implications for subduction zone chemical fluxes. *Journal of Petrology*, *49*(3), 523–553. https://doi.org/10.1093/petrology/egn001

Langston, C. A. (1979). Structure under Mount Rainier, Washington, inferred from teleseismic body waves. *Journal of Geophysical Research*, *84*(B9), 4749–4762. https://doi.org/10.1029/JB084iB09p04749

Lawrence, J. F., & Shearer, P. M. (2006). A global study of transition zone thickness using receiver functions. *Journal of Geophysical Research*, *111*(B6). https://doi.org/10.1029/2005JB003973

Leahy, G. M., & Bercovici, D. (2007). On the dynamics of a hydrous melt layer above the transition zone. *Journal of Geophysical Research*, *112*(7), 1–14. https://doi.org/10.1029/2006JB004631

Leahy, G. M., & Bercovici, D. (2010). Reactive infiltration of hydrous melt above the mantle transition zone. *Journal of Geophysical Research*, *115*(8), 1–17. https://doi.org/10.1029/2009JB006757

Li, H., Xu, Y., Ryan, J. G., Huang, X., Ren, Z., Guo, H., & Ning, Z. (2016). Olivine and melt inclusion chemical constraints on the source of intracontinental basalts from the eastern North China Craton: Discrimination of contributions from the subducted Pacific slab. *Geochimica et Cosmochimica Acta*, *178*, 1–19. https://doi.org/10.1016/j.gca.2015.12.032

Li, S., Yang, W., Ke, S., Meng, X., Tian, H., Xu, L., & Yan, J. (2017). Deep carbon cycles constrained by a large-scale mantle Mg isotope anomaly in eastern China. *National Science Review*, *4*(1), 111–120. https://doi.org/10.1093/nsr/nww070

Liu, Z., Park, J., & Karato, S. (2016). Seismological detection of low-velocity anomalies surrounding the mantle transition zone in Japan subduction zone. *Geophysical Research Letters*, *43*(6), 2480–2487. https://doi.org/10.1002/2015GL067097

Long, X., Ballmer, M. D., Córdoba, A. M., & Li, C. (2019). Mantle melting and intraplate volcanism due to self-buoyant hydrous upwellings from the stagnant slab that are conveyed by small-scale convection. *Geochemistry, Geophysics, Geosystems*, *20*(11), 4972–4997. https://doi.org/10.1029/2019GC008591

Ma, Q., & Xu, Y. (2021). Magmatic perspective on subduction of Paleo-Pacific plate and initiation of big mantle wedge in East Asia. *Earth-Science Reviews*, *213*, 103473. https://doi.org/10.1016/j.earscirev.2020.103473

Mazza, S. E., Gazel, E., Bizimis, M., Moucha, R., Beguelin, P., Johnson, E. A., & Sobolev, A. V. (2019). Sampling the volatile-rich transition zone beneath Bermuda. *Nature*, *569*(7756), 398–403. https://doi.org/10.1038/s41586-019-1183-6

McDonough, W. F., & Sun, S. S. (1995). The composition of the Earth. *Chemical Geology*, *120*(3–4), 223–253. https://doi.org/10.1016/0009-2541(94)00140-4

Motoki, M. H., & Ballmer, M. D. (2015). Intraplate volcanism due to convective instability of stagnant slabs in the mantle transition zone. *Geochemistry, Geophysics, Geosystems*, *16*(2), 538–551. https://doi.org/10.1002/2014GC005608

Obayashi, M., Sugioka, H., Yoshimitsu, J., & Fukao, Y. (2006). High temperature anomalies oceanward of subducting slabs at the 410-km discontinuity. *Earth and Planetary Science Letters*, *243*(1–2), 149–158. https://doi.org/10.1016/j.epsl.2005.12.032

Ohtani, E., Litasov, K., Hosoya, T., Kubo, T., & Kondo, T. (2004). Water transport into the deep mantle and formation of a hydrous transition zone. *Physics of the Earth and Planetary Interiors*, *143*, 255–269. https://doi.org/10.1016/j.pepi.2003.09.015

Plank, T. (2014). The chemical composition of subducting sediments. *Treatise on Geochemistry*, *4*, 607–629. https://doi.org/10.1016/B978-0-08-095975-7.00319-3

Plank, T., Kelley, K. A., Zimmer, M. M., Hauri, E. H., & Wallace, P. J. (2013). Why do mafic arc magmas contain ~4 wt% water on average? *Earth and Planetary Science Letters*, *364*, 168–179. https://doi.org/10.1016/j.epsl.2012.11.044

Plank, T., & Manning, C. E. (2019). Subducting carbon. *Nature*, *574*(7778), 343–352. https://doi.org/10.1038/s41586-019-1643-z

Qian, S., Nichols, A. R. L., Zhang, L., Xu, Y., Li, J., Guo, Y., & Ren, Z. (2020). The mantle transition zone hosts the missing HIMU reservoir beneath eastern China. *Geophysical Research Letters*, *47*(9), e2020GL087260. https://doi.org/10.1029/2020gl087260

Revenaugh, J., & Sipkin, S. A. (1994). Seismic evidence for silicate melt atop the 410-km mantle discontinuity. *Nature*, *369*(6480), 474–476. https://doi.org/10.1038/369474a0

Rohrbach, A., & Schmidt, M. W. (2011). Redox freezing and melting in the Earth's deep mantle resulting from carbon-iron redox coupling. *Nature*, *472*(7342), 209–212. https://doi.org/10.1038/nature09899

Schmandt, B., & Humphreys, E. (2011). Seismically imaged relict slab from the 55 Ma Siletzia accretion to the northwest United States. *Geology*, *39*(2), 175–178. https://doi.org/10.1130/g31558.1

Shirey, S. B., Wagner, L. S., Walter, M. J., Pearson, D. G., & van Keken, P. E. (2021). Slab transport of fluids to deep focus earthquake depths: Thermal modeling constraints and evidence from diamonds. *AGU Advances*, *2*(2), e2020AV000304. https://doi.org/10.1029/2021AV000434

Song, T.-R. A., Helmberger, D. V., & Grand, S. P. (2004). Low-velocity zone atop the 410-km seismic discontinuity in the northwestern United States. *Nature*, *427*(6974), 530–533. https://doi.org/10.1038/nature02231

Spiegelman, M., Kelemen, P. B., & Aharonov, E. (2001). Causes and consequences of flow organization during melt transport: The reaction infiltration instability in compactible media. *Journal of Geophysical Research*, *106*(B2), 2061–2077. https://doi.org/10.1029/2000JB900240

Stacey, J. S., & Kramers, J. D. (1975). Approximation of terrestrial lead isotope evolution by a two-stage model. *Earth and Planetary Science Letters*, *26*(2), 207–221. https://doi.org/10.1016/0012-821x(75)90088-6

Stracke, A., Hofmann, A. W., & Hart, S. R. (2005). FOZO, HIMU, and the rest of the mantle zoo. *Geochemistry, Geophysics, Geosystems*, *6*(5), Q05007. https://doi.org/10.1029/2004gc000824

Sun, C., & Dasgupta, R. (2019). Slab–mantle interaction, carbon transport, and kimberlite generation in the deep upper mantle. *Earth and Planetary Science Letters*, *506*, 38–52. https://doi.org/10.1016/j.epsl.2018.10.028

Sun, Y., Hier-Majumder, S., Xu, Y., & Walter, M. (2020). Stability and migration of slab-derived carbonate-rich melts above the transition zone. *Earth and Planetary Science Letters*, *531*, 116000. https://doi.org/10.1016/j.epsl.2019.116000

Sun, Y., Payton, R. L., Hier-Majumder, S., & Kingdon, A. (2020). Geological carbon sequestration by reactive infiltration instability. *Frontiers of Earth Science*, *8*, 533588. https://doi.org/10.3389/feart.2020.533588

Tauzin, B., Debayle, E., & Wittlinger, G. (2008). The mantle transition zone as seen by global Pds phases: No clear evidence for a thin transition zone beneath hotspots. *Journal of Geophysical Research*, *113*(B8). https://doi.org/10.1029/2007JB005364

Tauzin, B., Debayle, E., & Wittlinger, G. (2010). Seismic evidence for a global low-velocity layer within the Earth's upper mantle. *Nature Geoscience*, *3*(10), 718–721. https://doi.org/10.1038/ngeo969

Tauzin, B., Kim, S., & Kennett, B. (2017). Pervasive seismic low-velocity zones within stagnant plates in the mantle transition zone: Thermal or compositional origin? *Earth and Planetary Science Letters*, *477*, 1–13. https://doi.org/10.1016/j.epsl.2017.08.006

Tauzin, B., & Ricard, Y. (2014). Seismically deduced thermodynamics phase diagrams for the mantle transition zone. *Earth and Planetary Science Letters*, *401*, 337–346. https://doi.org/10.1016/j.epsl.2014.05.039

Tauzin, B., van der Hilst, R. D., Wittlinger, G., & Ricard, Y. (2013). Multiple transition zone seismic discontinuities and low velocity layers below western united states. *Journal of Geophysical Research*, *118*(5), 2307–2322. https://doi.org/10.1002/jgrb.50182

Thomson, A. R., Kohn, S. C., Bulanova, G. P., Smith, C. B., Araujo, D., & Walter, M. J. (2016). Trace element composition of silicate inclusions in sub-lithospheric diamonds from the Juina-5 kimberlite: Evidence for diamond growth from slab melts. *Lithos*, *265*, 108–124. https://doi.org/10.1016/j.lithos.2016.08.035

Thomson, A. R., Kohn, S. C., Bulanova, G. P., Smith, C. B., Araujo, D. P. E., & Walter, M. J. (2014). Origin of sublithospheric diamonds from the Juina-5 kimberlite (Brazil): Constraints from carbon isotopes and inclusion compositions. *Contributions to Mineralogy and Petrology*, *168*, 1081. https://doi.org/10.1007/s00410-014-1081-8

Thomson, A. R., Kohn, S. C., Prabhu, A., & Walter, M. J. (2021). Evaluating the formation pressure of diamond-hosted majoritic garnets: A machine learning majorite barometer. *Journal of Geophysical Research: Solid Earth*, *126*(3), e2020JB020604. https://doi.org/10.1029/2020JB020604

Thomson, A. R., Walter, M. J., Kohn, S. C., & Brooker, R. A. (2016). Slab melting as a barrier to deep carbon subduction. *Nature*, *529*(7584), 76–79. https://doi.org/10.1038/nature16174

Turcotte, D., & Schubert, G. (2002). *Geodynamics*. Cambridge University Press.

van Keken, P. E., Hacker, B. R., Syracuse, E. M., & Abers, G. A. (2011). Subduction factory: 4. Depth-dependent flux of H_2O from subducting slabs worldwide. *Journal of Geophysical Research*, *116*(B1), B01401. https://doi.org/10.1029/2010JB007922

Vinnik, L. (1977). Detection of waves converted from P to SV in mantle. *Physics of the Earth and Planetary Interiors*, *15*(1), 39–45. https://doi.org/10.1016/0031-9201(77)90008-5

Vinnik, L., & Farra, V. (2002). Subcratonic low-velocity layer and flood basalts. *Geophysical Research Letters*, *29*(4), 8–1. https://doi.org/10.1029/2001GL014064

Vinnik, L., & Farra, V. (2007). Low S velocity atop the 410-km discontinuity and mantle plumes. *Earth and Planetary Science Letters*, *262*(3–4), 398–412. https://doi.org/10.1016/j.epsl.2007.07.051

Walter, M. J., Bulanova, G. P., Armstrong, L. S., Keshav, S., Blundy, J. D., Gudfinnsson, G., & Gobbo, L. (2008). Primary carbonatite melt from deeply subducted oceanic crust. *Nature*, *454*(7204), 622–625. https://doi.org/10.1038/nature07132

Wei, S. S., & Shearer, P. M. (2017). A sporadic low-velocity layer atop the 410 km discontinuity beneath the Pacific Ocean. *Journal of Geophysical Research: Solid Earth*, *122*(7), 5144–5159. https://doi.org/10.1002/2017JB014100

Weiss, Y., Class, C., Goldstein, S. L., & Hanyu, T. (2016). Key new pieces of the HIMU puzzle from olivines and diamond inclusions. *Nature*, *537*(7622), 666–670. https://doi.org/10.1038/nature19113

Xiao, J., Hier-Majumder, S., Tauzin, B., & Waltham, D. (2020). An inversion approach for analysing the physical properties of a seismic low-velocity layer in the upper mantle. *Physics of the Earth and Planetary Interiors*, *304*, 106502. https://doi.org/10.1016/j.pepi.2020.106502

Xu, W., Lithgow-Bertelloni, C., Stixrude, L., & Ritsema, J. (2008). The effect of bulk composition and temperature on mantle seismic structure. *Earth and Planetary Science Letters*, *275*(1), 70–79. https://doi.org/10.1016/j.epsl.2008.08.012

Xu, Y., Zhang, H., Qiu, H., Ge, W., & Wu, F. (2012). Oceanic crust components in continental basalts from Shuangliao, Northeast China: Derived from the mantle transition zone? *Chemical Geology*, *328*, 168–184. https://doi.org/10.1016/j.chemgeo.2012.01.027

Zhang, Y., Wang, C., & Jin, Z. (2020). Decarbonation of stagnant slab in the mantle transition zone. *Journal of Geophysical Research: Solid Earth*, *125*(7), 1–19. https://doi.org/10.1029/2020JB019533

References From the Supporting Information

Clift, P. D. (2017). A revised budget for Cenozoic sedimentary carbon subduction. *Reviews of Geophysics*, *55*(1), 97–125. https://doi.org/10.1002/2016RG000531

Desmaele, E., Sator, N., Vuilleumier, R., & Guillot, B. (2019). The $MgCO_3$-$CaCO_3$-Li_2CO_3-Na_2CO_3-K_2CO_3 melts: Thermodynamics and transport properties by atomistic simulations. *The Journal of Chemical Physics*, *150*(21), 214503. https://doi.org/10.1063/1.5099015

Genge, M. J., Price, G. D., & Jones, A. P. (1995). Molecular dynamics simulations of $CaCO_3$ melts to mantle pressures and temperatures: Implications for carbonatite magmas. *Earth and Planetary Science Letters*, *131*(3–4), 225–238. https://doi.org/10.1016/0012-821X(95)00020-D

Hier-Majumder, S. (2020). *sashgeophysics/mupopp: Mupopp v1.2.1*. Zenodo. https://doi.org/10.5281/zenodo.3692431

Minarik, W., & Watson, E. B. (1995). Interconnectivity of carbonate melt at low melt fraction. *Earth and Planetary Science Letters*, *133*(3–4), 423–437. https://doi.org/10.1016/0012-821X(95)00085-Q

Sobolev, A. V., Hofmann, A. W., Kuzmin, D. V., Yaxley, G. M., Arndt, N. T., Chung, S.-L., & Teklay, M. (2007). The amount of recycled crust in sources of mantle-derived melts. *Science*, *316*(5823), 412–417. https://doi.org/10.1126/science.1138113

Spiegelman, M., & Kenyon, P. (1992). The requirements for chemical disequilibrium during magma migration. *Earth and Planetary Science Letters*, *109*(3–4), 611–620. https://doi.org/10.1016/0012-821X(92)90119-G

Wimert, J., & Hier-Majumder, S. (2012). A three-dimensional microgeodynamic model of melt geometry in the Earth's deep interior. *Journal of Geophysical Research*, *117*(B4). https://doi.org/10.1029/2011JB009012

Xu, M., Jing, Z., Bajgain, S. K., Mookherjee, M., Orman, J. A., Yu, T., & Wang, Y. (2020). High-pressure elastic properties of dolomite melt supporting carbonate-induced melting in deep upper mantle. *Proceedings of the National Academy of Sciences of the USA*, *117*(31), 18285–18291. https://doi.org/10.1073/pnas.2004347117